nanomaterials

MDPI

Article

Efficient Near-Infrared-Activated Photocatalytic Hydrogen Evolution from Ammonia Borane with Core-Shell Upconversion-Semiconductor Hybrid Nanostructures

Andrew J. Evangelista, Mariia Ivanchenko and Hao Jing *

Department of Chemistry and Biochemistry, George Mason University, Fairfax, VA 22030, USA; aevange3@gmu.edu (A.J.E.); mivanch@gmu.edu (M.I.)
* Correspondence: hjing2@gmu.edu

Abstract: In this work, the photocatalytic hydrogen evolution from ammonia borane under near-infrared laser irradiation at ambient temperature was demonstrated by using the novel core-shell upconversion-semiconductor hybrid nanostructures ($NaGdF_4$:Yb^{3+}/Er^{3+}@$NaGdF_4$@Cu_2O). The particles were successfully synthesized in a final concentration of 10 mg/mL. The particles were characterized via high resolution transmission electron microscopy (HRTEM), photoluminescence, energy dispersive X-ray analysis (EDAX), and powder X-ray diffraction. The near-infrared-driven photocatalytic activities of such hybrid nanoparticles are remarkably higher than that with bare upconversion nanoparticles (UCNPs) under the same irradiation. The upconverted photoluminescence of UCNPs efficiently reabsorbed by Cu_2O promotes the charge separation in the semiconducting shell, and facilitates the formation of photoinduced electrons and hydroxyl radicals generated via the reaction between H_2O and holes. Both serve as reactive species on the dissociation of the weak B-N bond in an aqueous medium, to produce hydrogen under near-infrared excitation, resulting in enhanced photocatalytic activities. The photocatalyst of $NaGdF_4$:Yb^{3+}/Er^{3+}@$NaGdF_4$@Cu_2O ($UCNPs@Cu_2O$) suffered no loss of efficacy after several cycles. This work sheds light on the rational design of near-infrared-activated photocatalysts, and can be used as a proof-of-concept for on-board hydrogen generation from ammonia borane under near-infrared illumination, with the aim of green energy suppliers.

Keywords: near-infrared; hydrogen evolution; upconversion; semiconductor; core-shell

Citation: Evangelista, A.J.; Ivanchenko, M.; Jing, H. Efficient Near-Infrared-Activated Photocatalytic Hydrogen Evolution from Ammonia Borane with Core-Shell Upconversion-Semiconductor Hybrid Nanostructures. *Nanomaterials* **2021**, *11*, 3237. https://doi.org/10.3390/nano11123237

Academic Editors: Laeticia Petit, Rajesh Komban and Antonino Gulino

Received: 16 November 2021
Accepted: 26 November 2021
Published: 29 November 2021

1. Introduction

Due to the extensive production of air-based pollution and the ultimately limited supply of fossil fuels, a search for a suitable fuel replacement is a priority. Switching to a clean source of energy is urgent because of the amount of damage the atmosphere has already suffered. In the search to replace fossil fuels with a cleaner alternative, hydrogen has emerged as a high potential candidate. Hydrogen is attractive due to its high chemical energy density and its ability to be stored in the three phases of matter: solid, liquid, and gas. Additionally, when produced from a clean and renewable source, the hydrogen producing reaction can have virtually zero emissions [1].

Owing to the explosive nature of gaseous hydrogen, and the immense pressure and sealing necessary to store liquid hydrogen, solid storage materials have gained significant traction [2–4]. In particular, chemically stored hydrogen, such as solid hydride complexes, specifically borohydride complexes, have been theorized as a possible solution [5–7]. For a while, sodium borohydride was the most popular choice for solid storage, since it could be used as an aqueous fuel independently, in a direct fuel cell, or direct liquid-free cell [8,9]. However, in 2007, the United States Department of Energy recommended that sodium borohydride not be used for on-board applications, such as for an automobile or a portable power pack [10]. Instead, ammonia borane (AB) was identified as a promising alternative,

by virtue of its remarkable gravimetric hydrogen storage capacity of 19.5 wt % and high stability in solid state at ambient temperature [11,12]. The catalytic decomposition of ammonia borane to produce hydrogen has drawn much attention in recent years [13–25]. Although various approaches were used to release hydrogen from AB over the years [26–37], there has been little that allows the claim of a practical application, due to the harsh conditions, such as high temperature during thermolysis and slow kinetics of dehydrogenation. To circumvent these issues, the exploitation of environmentally friendly technologies becomes imperative in the modern climate. Compared to other approaches, photocatalysis is superior, and is widely applied in photodegradation and photo-oxidization, as it utilizes the inexhaustible solar energy, while not generating hazardous pollutants. Inspired by the Fujishima Honda Effect reported in 1972 [38], a plethora of semiconductor-based photocatalysts, such as TiO_2, g-C_3N_4, CdS [39], various perovskites [40–55], and WO_3/rGO [56] have been utilized in hydrogen production. Additionally, non-semiconductor catalysts based on metals including platinium [57], rhenium [58], ruthenium [59,60], and iridium [61] have also been used in the catalytic generation of H_2 [62,63]. For these photocatalysts with their light absorption threshold confined in either ultraviolet (UV, 300–400 nm) or visible (VIS, 400–700 nm) region [64], the major limitation is that only UV and/or visible light photons can be utilized, which accounts for 5% and 43% of the full solar spectrum, respectively. The under-exploitation of more abundant low-energy near-infrared (NIR) light, which makes up 52% of the solar energy, undoubtedly imposes intrinsic limitations to the maximum achievable solar energy conversion efficiency, and hinders the practical application in the field of solar-to-fuels energy conversion. Although metallic or multi-metallic nanoparticles with geometrically tunable localized surface plasmon resonances (LSPRs) redshifted to NIR region, materials including ruthenium, platinum, palladium, cobalt, iron, nickel, silver [65–75], cadmium and tungsten [76], gold [77], and copper [78–82] were used for efficient H_2 generation; the inherent photo-corrosion susceptibility and inevitable high processing cost make their performance less satisfactory. Therefore, it is of great significance to design and develop more efficient photocatalysts with capabilities to utilize NIR light energy for stable photocatalytic H_2 production.

One promising tactic to improve the utilization of the low-energy NIR light to drive H_2 evolution is coupling nonlinear optical materials that can strongly absorb NIR light photons with a photocatalytic semiconductor. Among them, lanthanide-doped upconversion nanoparticles with well-controlled structures and morphologies are considered efficient candidates due to their unique and remarkable optical characteristics, such as their ability to convert near-infrared incident light into high-energy ultraviolet or visible light photons, large anti-Stokes shifts, sharp and tunable multi-peak line emission profiles, and excellent photostability [83–88]. Subsequently, the upconverted light photons need to be reabsorbed by the appropriate semiconductors, with a concomitant injection of electrons from the valance band (VB) to the conduction band (CB) of the semiconductor to generate photoinduced carriers. In this work, for the first time, we report the synthesis and characterization of core-shell UCNPs-semiconductor ($NaGdF_4$: Yb^{3+}/Er^{3+}@ $NaGdF_4$ @Cu_2O) hybrid nanostructures, and demonstrate the NIR-driven photocatalytic activities for H_2 evolution from ammonia borane (AB) molecules. Cuprous oxide (Cu_2O), a p-type semiconductor with high optical absorption coefficients, has a bulk band gap of ~2.2 eV [89–91]. This interesting exitonic feature ensures the spectral overlapping between absorption of Cu_2O and emission bands of UCNPs, which results in efficient energy transfer from UCNPs to Cu_2O through the reabsorbing of upconverted light photons. Integrating UCNPs and Cu_2O into one nano-entity with core-shell morphology efficiently promotes the direct energy migration under NIR light irradiation for the formation of photoinduced charge carriers, due to the intimate contact of two distinct materials. We can envision that this paradigm will provide new insights for the rational design of NIR-responsive photocatalysts, and reveal a new way for exploitation of sustainable energy sources.

2. Materials and Methods

2.1. Materials

Gadolinium (III) acetate hydrate (99.9%) ($Gd(OAc)_3$), ytterbium (III) acetate hydrate (99.9%) ($Yb(OAc)_3$), erbium (III) acetate hydrate (99.9%) ($Er(OAc)_3$), oleic acid (90%) (OA), 1-octadecene (90%) (1-ODE), sodium hydroxide (≥98%) (NaOH), ammonium fluoride (99.9%) (NH_4F), methanol (99.9%) (MeOH), cyclohexane (99.5%) (CH), nitrosyl tetrafluoroborate (95%) ($NOBF_4$), chloroform (99%) ($CHCl_3$), dimethylformamide (99.8%) (DMF), copper (II) nitrate (99.999%) ($Cu(NO_3)_2$), hydrazine (35 wt % in H_2O) (N_2H_4), 2-propanol (C_3H_8O), and ammonia borane (90%) (AB) were all purchased from Sigma Aldrich (St. Louis, MO, USA) and used without further purification. Ethanol (EtOH) was purchased from VWR and used as is. Ultrapure water (18.2 MΩ·cm resistivity, PURELAB Ultra Ionic Polishing system) was used for all experiments.

2.2. Characterization

The size and morphology of the nanoparticles were determined by using a Titan 80–300 analytical transmission electron microscope (TEM) (FEI Company, Hillsboro, OR, USA) operating at 300 kV. The standard TEM samples were prepared by dropping solutions of nanoparticles onto the surface of copper grids. Upconversion luminescence (UCL) spectra were recorded at room temperature on a high sensitivity QE Pro-FL spectrofluorometer (Ocean Optics, Inc, Dunedin, FL, USA), with the excitation source of an external 0–5 W adjustable continuous wave 980 nm laser diode (Dragon Lasers, China). Hydrogen evolution was tracked using a HP 5890 gas chromatograph (Hewlett-Packard, Palo Alto, CA, USA), equipped with a molecular sieve column and a thermal conductivity detector (TCD). The column had a 15 m length, a 0.530 mm diameter, and a 25.0 μm film. Energy dispersive X-ray spectroscopy (EDX) measurements were obtained on JSM-IT500HR scanning electron microscope (SEM) (JEOL USA, Inc, Peabody, MA, USA) equipped with an EDAX APEX detector (AMETEK, Inc., Berwyn, PA, USA). Powder X-ray diffraction (XRD) of the sample was measured at room temperature for 2 h with the scattering angle 2θ range from 20° to 80°, using a benchtop Miniflex-600 powder X-ray diffractometer (Cu Kα, λ = 1.5418 Å) (Rigaku Americas Corporation, The Woodlands, TX, USA). Size distribution/histogram was obtained using ImageJ software after measuring ~100 nanoparticles.

2.3. Photocatalytic H_2 Evolution

First, the semiconductor-coated UCNPs (0.5 mL, 1.26 mL, 2 mL) were added to a solution of ammonia borane (10 mL, 0.1 M) in a glass photoreactor equipped with a water jacket and quartz top. The water circulating in the jacket was kept at 20 °C to prevent the thermal decomposition of the ammonia borane. The solution was degassed with argon for 30 min. The photoreactor was then sealed and a 980 nm laser was introduced at 1 W. A 100 μL sample was taken every 30 min, for 180 min. To study the roles of hydroxyl radicals in the photcatalytic evolution of H_2, 2-propanol (0.1 mL) was added to the mixture in the presence of 2.0 mL semiconductor-coated UCNPs and 10 mL 0.1 M ammonium borane. Other conditions were the same as mentioned above for the photocatalysis.

2.4. Synthesis of $NaGdF_4$:Yb^{3+}/Er^{3+} UCNPs

First, $Gd(OAc)_3$ (67 mg), $Yb(OAc)_3$ (83 mg), $Er(OAc)_3$ (4.6 mg), oleic acid (4 mL) and 1-ODE (6 mL) were added to a 50 mL 3-neck flask. The flask was put under argon protection and heated to 150 °C with magnetic stirring. At temperature, vacuum was pulled to remove oxygen, moisture, and other low boiling point impurities. After several degas cycles, the reaction was cooled to 50 °C. At this point, a mixture of NaOH (50 mg) and NH_4F (70 mg) dissolved in 10 mL of methanol was added and stirred for 30 min. Next, the solution was degassed for several cycles at various temperatures (70 °C, 100 °C, 150 °C) to remove the methanol, and any other lower boiling point impurities. The reaction solution was then heated to 290 °C, and allowed to react for 90 min. After cooling, the mixture was spun in a centrifuge at 6000 rpm for 4 min and washed once with ethanol

(5 mL), and then spun again and washed with a mixture of ethanol (8 mL) and cyclohexane (4 mL). After a final spin, the particles were redispersed in cyclohexane (4 mL).

2.5. Synthesis of Hydrophobic Core-Shell $NaGdF_4$:Yb^{3+}/Er^{3+}@$NaGdF_4$ UCNPs

To start, the previously synthesized cores $NaGdF_4$:Yb^{3+}/Er^{3+}, in cyclohexane (4 mL), were added to a 50 mL 3-neck flask, along with $Gd(OAc)_3$ (134 mg), oleic acid (4 mL), and 1-ODE (6 mL). The flask was put under argon protection with magnetic stirring, and the mixture was degassed at 150 °C. Once the reaction naturally cooled to 50 °C, both NaOH (1 mL, 1.0 M in methanol) and NH_4F (3.33 mL, 0.4 M in methanol) were added. The reaction mixture was stirred for 30 min and was then degassed again at 70 °C, 100 °C, and 150 °C, to remove methanol and other low boiling point impurities. The temperature was increased to 290 °C, and the reaction was allowed to stir for 90 min. Upon cooling to room temperature, the reaction solution was washed by the same procedure as the core particles. The final dispersion was in 4 mL of cyclohexane.

2.6. Transformation to Hydrophilic $NaGdF_4$:Yb^{3+}/Er^{3+}@$NaGdF_4$ UCNPs

The core/shell UCNPs ($NaGdF_4$:Yb^{3+}/Er^{3+}@$NaGdF_4$), in cyclohexane (2 mL), were mixed with $NOBF_4$ (2 mL, 50 mM in DMF). The combination was sonicated for 30 min, and the layers were allowed to separate. The cyclohexane layer was removed, and chloroform (8 mL) was added to the hydrophilic layer. The solution was centrifuged at 6000 rpm for 5 min. The pellet was then redispersed in 2 mL of DMF.

2.7. Synthesis of $NaGdF_4$:Yb^{3+}/Er^{3+}@$NaGdF_4$@Cu_2O UCNPs

The hydrophilic UCNPs ($NaGdF_4$:Yb^{3+}/Er^{3+}@$NaGdF_4$), in DMF (2 mL), were added to a reaction vial with magnetic stirring. A 25 mM solution of $Cu(NO_3)_2$ (3.2 mL) was added dropwise, and the mixture stirred for 30 min. Next, NaOH (4.8 mL, 0.1 M) was added quickly, and the reaction was stirred for 30 more minutes. Then, N_2H_4 (4.8 mL, 0.1 M) was added dropwise, and the solution was allowed to stir for an additional 30 min. The reaction solution was transferred to an autoclave reactor with a Teflon liner, and was heated to 170 °C for 18 h. The solution was then spun in a centrifuge at 3000 rpm for 1 min to remove large particles, and then the supernatant was allowed to settle overnight. The remaining solution was then spun at 12,000 rpm for 20 min, and the pellet was redispersed in ultra-pure water (1 mL, 18 MΩ cm).

3. Results

After purification, the UCNPs were measured via TEM at each stage in the synthesis, to ensure uniformity in size and morphology. As shown in Figure 1A, the as-synthesized core UCNPs ($NaGdF_4$:Yb^{3+}/Er^{3+}) were single crystalline and highly monodisperse with spherical morphologies. The lattice fringes had d-spacings of 0.515 nm, corresponding to the (100) planes of ß-phase $NaGdF_4$:Yb^{3+}/Er^{3+}, as demonstrated in Figure 2B. The particle sizes were determined to be 20.9 nm ± 0.8 nm, based on the size distribution diagram obtained by measuring ~100 particles (Figure 1C). After epitaxially growing an inert shell of $NaGdF_4$ on the spherical core UCNPs, the sizes of core-shell UCNPs ($NaGdF_4$:Yb^{3+}/Er^{3+}@ $NaGdF_4$) increased slightly to 24.2 nm ± 1.1 nm, and the shapes and morphologies evolved to hexagons, confirmed by TEM images shown in Figure 2.

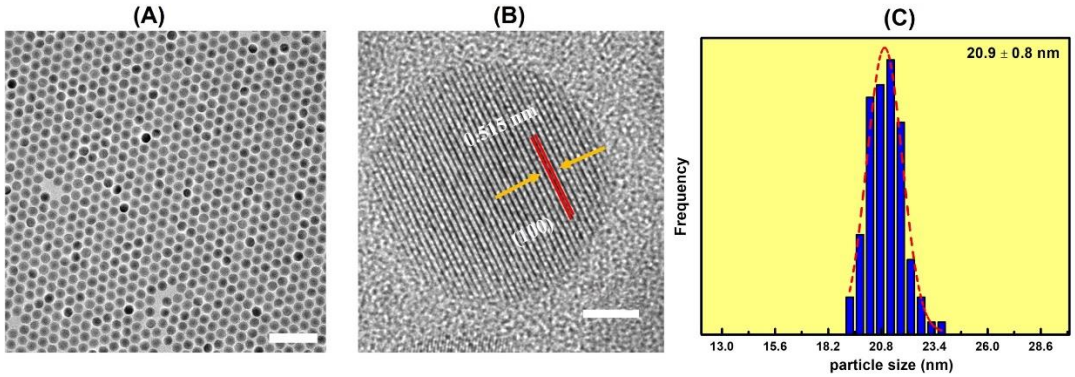

Figure 1. (**A**) A TEM image of $NaGdF_4$:Yb^{3+}/Er^{3+} particles, where both the hexagonal shape of the formation and the particles is evident. The scale bar is 100 nm. (**B**) An HRTEM image of a select $NaGdF_4$:Yb^{3+}/Er^{3+} particle, where the lattice fringes can be seen. The d-spacing was measured to be 0.515 nm, corresponding to the (100) face of ß-$NaGdF_4$:Yb^{3+}/Er^{3+}. The scale bar is 5 nm. (**C**) The size distribution diagram of the $NaGdF_4$:Yb^{3+}/Er^{3+} particles, measured from ~100 particles.

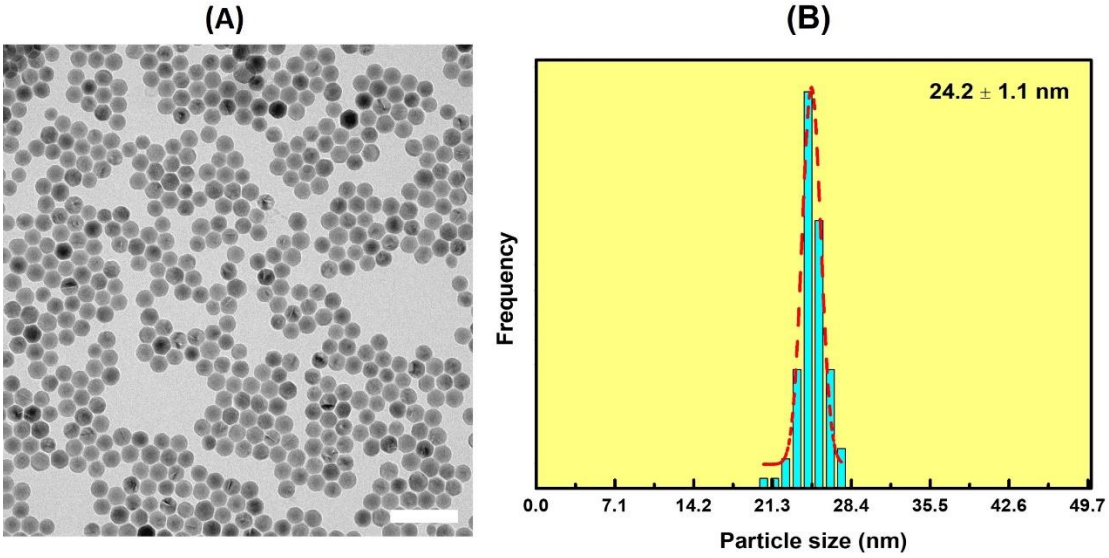

Figure 2. (**A**) A TEM image of $NaGdF_4$:Yb^{3+}/Er^{3+}@$NaGdF_4$. The scale bar is 100 nm. (**B**) The size distribution diagram of $NaGdF_4$:Yb^{3+}/Er^{3+}@$NaGdF_4$. The increase in size and uniformity can be noted here, due to the addition of the inert $NaGdF_4$ shell.

Subsequently, the thin layer of Cu_2O was successfully grown on the surface of ß-$NaGdF_4$:Yb^{3+}/Er^{3+}@$NaGdF_4$ to form eccentric core-shell UCNP-semiconductor hybrid heterostructures ($NaGdF_4$:Yb^{3+}/Er^{3+}@$NaGdF_4$@Cu_2O), with a facile and robust wet-chemistry approach, using an autoclave reactor with a Teflon liner, at a temperature of 170 °C for 18 h. The detailed structural information on ß-$NaGdF_4$:Yb^{3+}/Er^{3+}@$NaGdF_4$, the Cu_2O shell, as well as the interfaces between the core and shell, were clearly provided by the HRTEM measurements. As shown in Figure 3A, the shapes of the hybrid nanostructures changed from hexagons to quasi-spheres after Cu_2O was grown on the surface, and the surface roughness of the core-shell hybrid nanoparticles was clearly observed in the HRTEM image, due to the growth of the Cu_2O layer. The boundaries between the UCNP cores and the outer layer of Cu_2O were also resolved and highlighted by the white dashed line. The single zoomed in particle further confirmed the core-shell morphology and the atomically well-defined crystalline facets, with the lattice fringes showing interplanar distances of 0.52 nm and 0.21 nm, corresponding to the (200) planes of UCNPs and Cu_2O, respectively (Figure 3B). An additional high-resolution TEM image with interplanar spacings of the core and shell was shown (Figure S1) to further confirm the crystallographic planes of $NaGdF_4$ and

Cu_2O in the hybrid heteronanostructures. The crystal structures of the hybrid nanoparticles ($NaGdF_4$:Yb^{3+}/Er^{3+}@$NaGdF_4$@Cu_2O) were examined by X-ray powder diffraction (XRD) analysis (Figure S2). The characteristic diffraction peaks indexed to the pure hexagonal phase $NaGdF_4$ (JCPDS 27-0699) and Cu_2O (JCPDS 05-0667) further confirmed the core-shell structure synthesized. Meanwhile, the energy dispersive X-ray (EDX) spectroscopy analysis was performed to validify the chemical compositions (Figure S3).

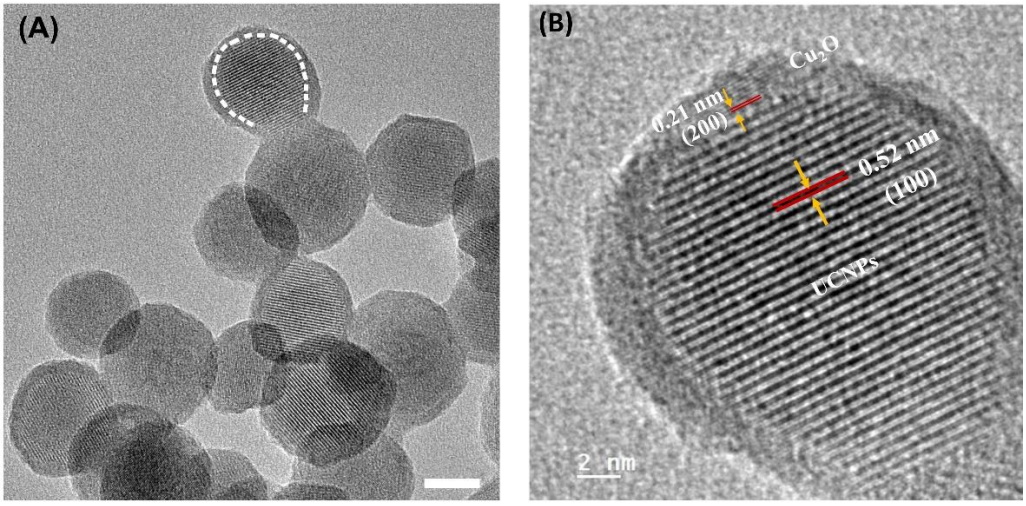

Figure 3. High resolution TEM images of (**A**) $NaGdF_4$: Yb^{3+}/Er^{3+}@ $NaGdF_4$ @Cu_2O, with the boundary between UCNPs and Cu_2O clearly observed and highlighted by a circular white dashed line and (**B**) a zoom-in of the particle outlined in (**A**). The fringes can be seen and a visual differentiation between the $NaGdF_4$ and the Cu_2O can be noted. Additionally, the d-spacing of each can be measured. They are 0.52 and 0.21, which correspond to the (100) facet of $NaGdF_4$ and (200) crystal plane of Cu_2O, respectively. The scale bars are (**A**) 10 nm and (**B**) 2 nm, respectively.

Figure 4 shows the upconversion photoluminescence spectra of $NaGdF_4$:Yb^{3+}/Er^{3+} (UCNPs core), hydrophobic (CSUCNPs in C_6H_{12}) and hydrophilic $NaGdF_4$:Yb^{3+}/Er^{3+}@$NaGdF_4$ (CSUCNPs in H_2O), and $NaGdF_4$:Yb^{3+}/Er^{3+}@$NaGdF_4$@Cu_2O (CSUCNPs@Cu_2O) hybrid nanostructures, under 980 nm NIR laser excitation. Three distinct non-radiative relaxations in the spectra were observed, including $^2H_{11/2} \rightarrow {}^4I_{15/2}$ (528 nm), $^4S_{3/2} \rightarrow {}^4I_{15/2}$ (541 nm) and $^4F_{9/2} \rightarrow {}^4I_{15/2}$ (656 nm), which was attributed to the transitions of erbium (Er^{3+}) ions after the pump photons were absorbed by ytterbium (Yb^{3+}) ions, and the energy was resonantly transferred to adjacent Er^{3+} in the matrix under the excitation. The peak intensities of the as-synthesized hydrophobic $NaGdF_4$:Yb^{3+}/Er^{3+}@$NaGdF_4$ were significantly increased after an inert layer of $NaGdF_4$ was grown, as shown by the red curve in Figure 4. During the transformation from hydrophobic to hydrophilic $NaGdF_4$:Yb^{3+}/Er^{3+}@$NaGdF_4$ dispersed in aqueous phase through a facile ligand-exchange method using $NOBF_4$, the photoluminescence emission intensities decreased, mainly due to the detrimental quenching effects of the H_2O molecules demonstrated by the blue curve in Figure 4. Upon the coating of the semiconductor Cu_2O layer, the photoluminescence of the hybrid $NaGdF_4$:Yb^{3+}/Er^{3+}@$NaGdF_4$@Cu_2O nanoparticles was almost quenched (pink curve), indicating the efficient energy transfer from UCNPs to the shell Cu_2O under 980 nm excitation. Cu_2O has a bulk band gap of ~2.2 eV, and its absorption spectrally overlaps with all three emission bands of the UCNPs, resulting in the reabsorption of the upconverted light photons, and the quenching of the upconverted photoluminescence of the core-shell hybrid hetero-nanostructures. It is noteworthy to point out that the intimate contact stemming from the core-shell structures facilitated the reabsorption of the upconverted photoluminescence emissions by Cu_2O, and the subsequent transition of the electrons in the valence band to the conduction band, which photo-catalyze the chemical transformations of ammonia borane (AB) for H_2 production.

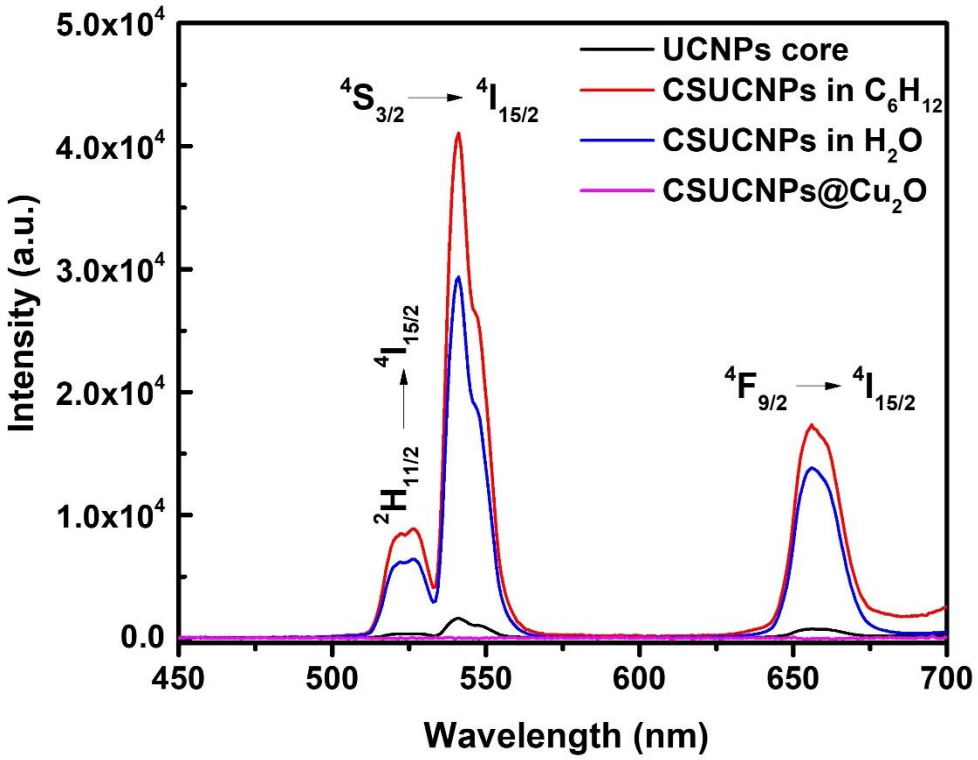

Figure 4. The photoluminescence spectra of the particles at various stages in the synthesis.

The photocatalytic activities of the hybrid $NaGdF_4:Yb^{3+}/Er^{3+}@NaGdF_4@Cu_2O$ ($CSUCNPs@Cu_2O$) nanostructures were investigated by H_2 evolution from the hydrolysis of AB (NH_3BH_3) under 980 nm NIR laser irradiation. The experimental setup was shown in Figure S4. As shown in Figure 5A, the photocatalytic H_2 production was quantified under various conditions by gas chromatography (GC) equipped with a TCD detector, including pure AB molecules irradiated by 980 nm NIR laser, pure AB molecules without irradiation of 980 nm NIR laser, bare UCNPs with excitation of 980 nm NIR laser, and AB molecules in the presence of three samples of $NaGdF_4:Yb^{3+}/Er^{3+}@NaGdF_4@Cu_2O$ ($UCNPs@Cu_2O$), with increasing volumes (0.5 mL, 1.3 mL and 2.0 mL) under illumination of 980 nm laser. It was demonstrated that the dehydrogenation of AB molecules barely occurred, with negligible amounts of H_2 being generated in the absence of photocatalysts ($NaGdF_4:Yb^{3+}/Er^{3+}@NaGdF_4@Cu_2O$), with and without 980 nm NIR laser irradiation, for a period of 3 h. In addition, slight reaction occurred in the presence of UCNPs without Cu_2O shells ($NaGdF_4:Yb^{3+}/Er^{3+}@NaGdF_4$), further confirming the stability of AB molecules in the photocatalytic experiments. The hydrolysis of AB was efficiently catalyzed by photocatalysts ($NaGdF_4:Yb^{3+}/Er^{3+}@NaGdF_4@Cu_2O$), and considerable amounts of H_2 were evolved and detected during the first hour of 980 nm NIR laser irradiation. The production of H_2 significantly increased over a period of 180 min under the excitation. The enhanced photocatalytic performance can be primarily ascribed to the energy transfer from UCNPs to the Cu_2O shell and the photoinduced charge carriers promoting the dehydrogenation of AB molecules under NIR excitation. With increasing amounts of $NaGdF_4:Yb^{3+}/Er^{3+}@NaGdF_4@Cu_2O$ (0.5 mL, 1.3 mL, and 2.0 mL), the photocatalytic H_2 production was boosted, indicated by the rise in the amounts of H_2 detected at each 30 min time intervals (Figure 5A). More importantly, core-shell $NaGdF_4:Yb^{3+}/Er^{3+}@NaGdF_4@Cu_2O$ nanoparticles exhibited exceptional NIR light-driven catalytic durability over multiple cycles of photocatalytic H_2 evolution (Figure 5B). It can clearly be seen that the photocatalysts suffered little to no loss of activity after three cycles, lasting 540 min, allowing for potential use in an onboard hydrogen application due to the well-preserved photocatalytic activities.

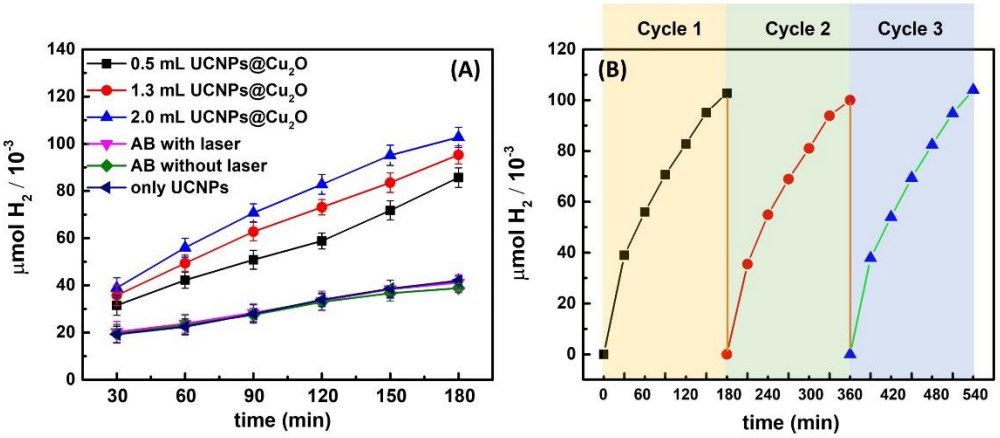

Figure 5. (**A**) H_2 production profiles from various photocatalytic conditions. Each reaction was kept at 20 °C and irradiated with a 980 nm NIR laser with the power intensity set to 1 W. (The concentrations are 0.476 mg/mL, 1.119 mg/mL, and 1.667 mg/mL for 0.5 mL, 1.3 mL and 2.0 mL of UCNPs@Cu_2O used, respectively). (**B**) Amount of H_2 produced over time on repeat cycles of the UCNP@Cu_2O to show reusability.

A schematic of the charge transfer process was proposed to illustrate the NIR-driven mechanism of photocatalytic H_2 evolution over the synthesized core-shell $NaGdF_4$:Yb^{3+}/Er^{3+}@$NaGdF_4$@Cu_2O hybrid nanostructures in Figure 6. Under the excitation of 980 nm NIR laser, three successive energy transfers ($^2H_{11/2} \rightarrow {}^4I_{15/2}$, $^4S_{3/2} \rightarrow {}^4I_{15/2}$ and $^4F_{9/2} \rightarrow {}^4I_{15/2}$) from the sensitizer Yb^{3+} ions to activator Er^{3+} ions occur, resulting in the emissions in ultraviolet (UV) and visible regions. These upconverted emissions are then reabsorbed by Cu_2O via an energy transfer process to generate photoexcited charge carriers. The band gap value of UCNPs@Cu_2O was determined to be ~2.25 eV according to the Tauc Plot (Figure S5). The photo-generated electrons are excited from the valence band (VB) to the conduction band (CB) of Cu_2O, while positively charged holes are left in the VB to react with H_2O molecules to form hydroxyl radicals. The intermediate of hydroxyl radicals is crucial in the investigation of the mechanism for the photocatalysis, and various methods were reported for the detection [92–95]. The formation of hydroxyl radicals was confirmed by the addition of 2-propanol acting as the hydroxyl radical scavenger during the photcatalytic H_2 evolution under 980 nm NIR laser irradiation. The photocatalytic activities significantly decreased for AB dehydrogenation in the presence of 2-propanol, due to the decrease of the concentration of hydroxyl radicals (Figure S6). Due to the electronegativity difference between B and N atoms, the polar and weak B-N chemical bond formed by sharing lone pair electrons between NH_3 and BH_3 moieties is susceptible to be attacked by both H_2O molecules and photogenerated electrons. In addition, during the transformation of as-synthesized hydrophobic UCNPs to hydrophilic ones, the surface of particles was capped by BF_4^- species. These negatively charged species were carried over to the surface of core-shell UCNPs@Cu_2O hybrid nanostructures, which facilitates the absorption of AB by the electrostatic interaction between the electron-deficient BH_3 moiety of the AB molecules and BF_4^- species, forming an activated complex species. We assume that the hydroxyl radicals and photoinduced electrons are both reactive species to enhance the catalytic H_2 evolution for AB dehydrogenation, by dissociating the weak B-N bond in aqueous medium.

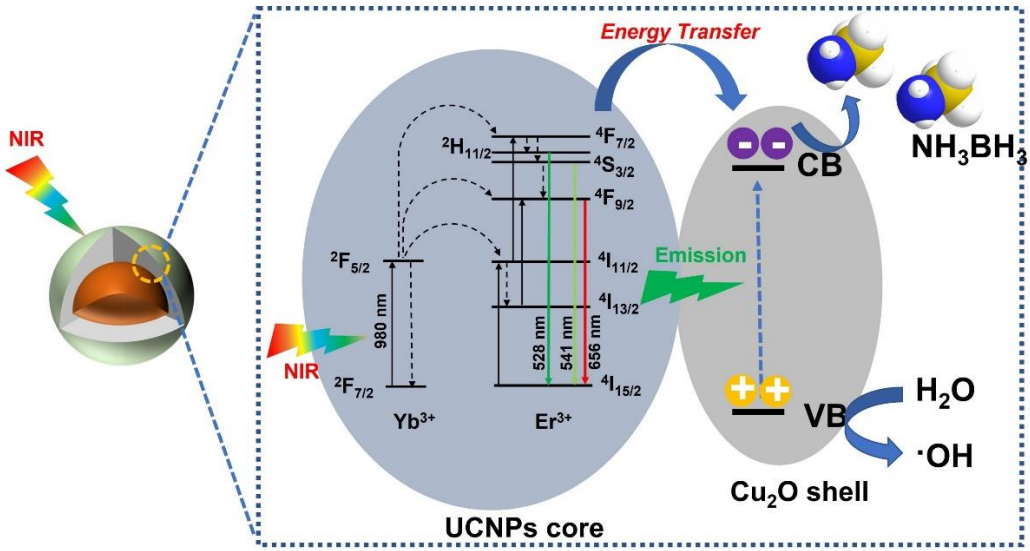

Figure 6. The mechanistic scheme for the transfer of energy from a source, through the particles, to the degradation of ammonia borane.

4. Conclusions

In summary, the novel ß-phase $NaGdF_4$:Yb^{3+}/Er^{3+}@$NaGdF_4$@Cu_2O core-shell hybrid nanoparticles were synthesized for the first time and successfully characterized with a concentration of 10 mg/mL. The intimate contact of the semiconducting shell to the core nanostructures led to an efficient energy transfer from the UCNPs to the Cu_2O under the excitation of a 980 nm laser, which subsequently generated photoinduced charge carriers actively participating in photocatalysis. The remarkable NIR-driven photocatalytic performance was then evaluated by H_2 evolution from the dehydrogenation of AB (NH_3BH_3) molecules under 980 nm laser irradiation. Upon reaction with AB molecules, the amount of H_2 produced drastically increased in the presence of the hybrid photocatalysts based on UCNPs and the semiconductor Cu_2O, compared to pure AB, with and without irradiation, as well as in conjunction with UCNPs without a semiconductor shell. In addition, the NIR-driven photocatalytic activities were highly stable over multiple uses in the recycling experiments. We speculate that this study can serve as the guideline for the rational design and development of NIR-responsive photocatalysts and provide a new direction for improving efficient near-infrared-activated photocatalytic H_2 production toward sustainable energy utilization in the near future.

Supplementary Materials: The following are available online at https://www.mdpi.com/article/10.3390/nano11123237/s1, Figure S1: Additional high-resolution TEM image of UCNPs@Cu_2O core-shell hybrid hetero-nanostructures. Figure S2: XRD patterns of $NaGdF_4$: Yb^{3+}/Er^{3+}@$NaGdF_4$@Cu_2O (UCNPs@Cu_2O). Figure S3: Energy-dispersive X-ray (EDX) spectra of core-shell $NaGdF_4$: Yb^{3+}/Er^{3+}@$NaGdF_4$@Cu_2O (UCNPs@Cu_2O) nanoparticles. Figure S4: The picture of the experimental setup for the photocatalytic H_2 evolution. Figure S5: Tauc plot of UCNPs@Cu_2O and UV-absorbance of UCNPs@Cu_2O core-shell hybrid hetero-nanostructures. Figure S6: The photocatalytic H_2 evolution from AB dehydrogenation over the time catalyzed by UCNPs@Cu_2O in the absence (black) and presence of 2-propanol (red) acting as the hydroxyl radical scavenger under 980 nm NIR laser irradiation.

Author Contributions: Conceptualization, H.J.; methodology, A.J.E.; formal analysis, A.J.E.; investigation, A.J.E.; data curation, M.I.; writing—original draft preparation, H.J. and A.J.E.; writing—review and editing, H.J., A.J.E. and M.I.; supervision, H.J.; funding acquisition, H.J. All authors have read and agreed to the published version of the manuscript.

Funding: This work was supported by Startup Foundation (101112) and College of Science (COS) Seed Grant (181282) of George Mason University.

Data Availability Statement: The data presented in this study are available on request from the corresponding author.

Acknowledgments: We acknowledge Alline F. Myers at the Center for Nanoscale Science and Technology (CNST) NanoFab, National Institute of Standards and Technology (NIST) for TEM technical support and helpful discussions. We also thank Zachary T. Messegee for the technical support on powder XRD analysis.

Conflicts of Interest: The authors declare no conflict of interest.

References

1. Motyka, T.; Zidan, R.; Summers, W.A. Hydrogen Storage: The Key Challenge Facing a Hydrogen Economy. United States Department of Energy 2004. Available online: http://citeseerx.ist.psu.edu/viewdoc/download?doi=10.1.1.194.5361&rep=rep1&type=pdf (accessed on 15 November 2021).
2. Staubitz, A.; Robertson, A.P.M.; Manners, I. Ammonia-Borane and Related Compounds as Dihydrogen Sources. *Chem. Rev.* **2010**, *110*, 4079–4124. [CrossRef] [PubMed]
3. Schlapbach, L.; Züttel, A. Hydrogen-Storage Materials for Mobile Applications. *Nature* **2001**, *414*, 353–358. [CrossRef]
4. Yadav, M.; Xu, Q. Liquid-Phase Chemical Hydrogen Storage Materials. *Energy Environ. Sci.* **2012**, *5*, 9698. [CrossRef]
5. Jain, I.P.; Jain, P.; Jain, A. Novel Hydrogen Storage Materials: A Review of Lightweight Complex Hydrides. *J. Alloys Compd.* **2010**, *503*, 303–339. [CrossRef]
6. Orimo, S.-I.; Nakamori, Y.; Eliseo, J.R.; Züttel, A.; Jensen, C.M. Complex Hydrides for Hydrogen Storage. *Chem. Rev.* **2007**, *107*, 4111–4132. [CrossRef]
7. Züttel, A.; Borgschulte, A.; Orimo, S.-I. Tetrahydroborates as New Hydrogen Storage Materials. *Scr. Mater.* **2007**, *56*, 823–828. [CrossRef]
8. Amendola, S.C.; Onnerud, P.; Kelly, M.T.; Petillo, P.J.; Sharp-Goldman, S.L.; Binder, M. A Novel High Power Density Borohydride-Air Cell. *J. Power Sources* **1999**, *84*, 130–133. [CrossRef]
9. Demirci, U.B.; Miele, P. Sodium Borohydride versus Ammonia Borane, in Hydrogen Storage and Direct Fuel Cell Applications. *Energy Environ. Sci.* **2009**, *2*, 627. [CrossRef]
10. U.S. Department of Energy. Go No-Go Recommendation for Sodium Borohydride for On-Board Vehicular Hydrogen Storage. 2007; NREL/MP-150-42220. Available online: https://www.hydrogen.energy.gov/pdfs/42220.pdf (accessed on 15 November 2021).
11. Jo, S.; Verma, P.; Kuwahara, Y.; Mori, K.; Choi, W.; Yamashita, H. Enhanced Hydrogen Production from Ammonia Borane Using Controlled Plasmonic Performance of Au Nanoparticles Deposited on TiO_2. *J. Mater. Chem. A* **2017**, *5*, 21883–21892. [CrossRef]
12. Stephens, F.H.; Pons, V.; Tom Baker, R. Ammonia–Borane: The Hydrogen Source Par Excellence? *Dalton Trans.* **2007**, *25*, 2613–2626. [CrossRef]
13. Coskuner, O.; Figen, A.K. Hydro-catalytic Treatment of Organoamine Boranes for Efficient Thermal Dehydrogenation for Hydrogen Production. *Int. J. Hydrogen Energy* **2021**, *46*, 35641–35652. [CrossRef]
14. Lv, H.; Wei, R.; Guo, X.W.; Sun, L.Z.; Liu, B. Synergistic Catalysis of Binary RuP Nanoclusters on Nitrogen-Functionalized Hollow Mesoporous Carbon in Hydrogen Production from the Hydrolysis of Ammonia Borane, J.P. *Chem. Lett.* **2021**, *12*, 696–703. [CrossRef]
15. Ren, X.Y.; Lv, H.; Yang, S.; Wang, Y.Y.; Li, J.L.; Wei, R.; Xu, D.D.; Liu, B. Promoting Effect of Heterostructured NiO/Ni on Pt Nanocatalysts Toward Catalytic Hydrolysis of Ammonia Borane. *J. Phys. Chem. Lett.* **2019**, *10*, 7374–7382. [CrossRef]
16. Wang, G.Q.; Wang, C.J.; Zhang, H.; Liu, Y.L.; Xu, J. Facile Preparation of Cu-Fe Oxide Nanoplates for Ammonia Borane Decomposition and Tandem Nitroarene Hydrogenation. *RSC Adv.* **2021**, *11*, 29920–29924. [CrossRef]
17. Wei, R.; Chen, Z.; Lv, H.; Zheng, X.; Ge, X.; Sun, L.; Song, K.; Kong, C.; Zhang, W.; Liu, B. Ultrafine RhNi Nanocatalysts Confined in Hollow Mesoporous Carbons for a Highly Efficient Hydrogen Production from Ammonia Borane. *Inorg. Chem.* **2021**, *60*, 6820–6828. [CrossRef]
18. Wang, Y.; Lv, H.; Grape, E.S.; Gaggioli, C.A.; Tayal, A.; Dharanipragada, A.; Willhammar, T.; Inge, A.K.; Zou, X.D.; Liu, B.; et al. A Tunable Multivariate Metal-Organic Framework as a Platform for Designing Photocatalysts. *J. Am Chem. Soc.* **2021**, *143*, 6333–6338. [CrossRef]
19. He, J.H.; Yao, Z.D.; Xiao, X.Z.; Chen, W.Z.; Huang, Z.W.; Fan, X.L.; Dong, Z.; Huang, X.; Wang, X.C.; Chen, M.; et al. Heterostructured Ni/NiO Nanoparticles on 1D Porous MoO_x for Hydrolysis of Ammonia Borane. *ACS Appl. Energy Mater.* **2021**, *4*, 1208–1217. [CrossRef]
20. Zhang, L.; Oishi, T.; Gao, L.Z.; Hu, S.Y.; Yang, L.L.; Li, W.; Wu, S.J.; Shang, R.; Yamamoto, Y.; Li, S.H.; et al. Catalytic Dehydrogenation of Ammonia Borane Mediated by a Pt(0)/Borane Frustrated Lewis Pair: Theoretical Design. *ChemPhysChem* **2020**, *21*, 2573–2578. [CrossRef]
21. Nagyhazi, M.; Turczel, G.; Anastas, P.T.; Tuba, R. Highly Efficient Ammonia Borane Hydrolytic Dehydrogenation in Neat Water Using Phase-Labeled CAAC-Ru Catalysts. *ACS Sustain. Chem. Eng.* **2020**, *8*, 16097–16103. [CrossRef]

22. Pei, P.; Cannon, M.; Quan, G.; Kjeang, E. Effective Hydrogen Release from Ammonia Borane and Sodium Borohydride Mixture Through Homopolar Based Dehydrocoupling Driven by Intermolecular Interaction and Restrained Water Supply. *J. Mater. Chem. A* **2020**, *8*, 19050–19056. [CrossRef]
23. Yao, Q.L.; Ding, Y.Y.; Lu, Z.H. Noble-metal-free Nanocatalysts for Hydrogen Generation from Boron- and Nitrogen-based Hydrides. *Inorg. Chem. Front.* **2020**, *7*, 3837–3874. [CrossRef]
24. Yuan, Y.; Chen, X.Y.; Zhang, X.; Wang, Z.M.; Yu, R.B. A MOF-derived CuCo(O)@Carbon-nitrogen Framework as an Efficient Synergistic Catalyst for the Hydrolysis of Ammonia Borane. *Inorg. Chem. Front.* **2020**, *7*, 2043–2049. [CrossRef]
25. Wang, Y.; Zou, K.L.; Zhang, D.; Li, G.D.; Meng, W.; Wang, D.; Cao, Z.Q.; Zhang, K.; Wu, S.W. Co-Mo-B Nanoparticles Supported on Carbon Cloth as Effective Catalysts for the Hydrolysis of Ammonia Borane. *Int. J. Hydrogen Energy* **2020**, *45*, 14418–14427. [CrossRef]
26. Principe, G.; Agresti, F.; Maddalena, A.; Russo, S.L. The Problem of Solid-State Hydrogen Storage. *Energy* **2009**, *34*, 2087–2091. [CrossRef]
27. Ares, J.R.; Aguey-Zinsou, K.-F.; Leardini, F.; Ferrer, I.J.; Fernandez, J.-F.; Guo, Z.-X.; Sánchez, C. Hydrogen Absorption/Desorption Mechanism in Potassium Alanate ($KAlH_4$) and Enhancement by $TiCl_3$ Doping. *J. Phys. Chem. C* **2009**, *113*, 6845–6851. [CrossRef]
28. Li, H.-W.; Yan, Y.; Orimo, S.-I.; Züttel, A.; Jensen, C.M. Recent Progress in Metal Borohydrides for Hydrogen Storage. *Energies* **2011**, *4*, 185–214. [CrossRef]
29. Bogdanovic, B.; Felderhoff, M.; Streukens, G. Hydrogen Storage in Complex Metal Hydrides. *J. Serb. Chem. Soc.* **2009**, *74*, 183–196. [CrossRef]
30. Aguey-Zinsou, K.-F.; Yao, J.; Guo, Z.X. Reaction Paths between LiNH2and LiH with Effects of Nitrides. *J. Phys. Chem. B* **2007**, *111*, 12531–12536. [CrossRef] [PubMed]
31. Xiong, Z.; Yong, C.K.; Wu, G.; Chen, P.; Shaw, W.; Karkamkar, A.; Autrey, T.; Jones, M.O.; Johnson, S.R.; Edwards, P.P.; et al. High-Capacity Hydrogen Storage in Lithium and Sodium Amidoboranes. *Nat. Mater.* **2008**, *7*, 138–141. [CrossRef]
32. Nakamori, Y.; Orimo, S.-I. Destabilization of Li-Based Complex Hydrides. *J. Alloys Compd.* **2004**, *370*, 271–275. [CrossRef]
33. Pinkerton, F.E.; Meyer, M.S.; Meisner, G.P.; Balogh, M.P.; Vajo, J.J. Phase Boundaries and Reversibility of $LiBH_4/MgH_2$ Hydrogen Storage Material. *J. Phys. Chem. C* **2007**, *111*, 12881–12885. [CrossRef]
34. Vajo, J.J.; Olson, G.L. Hydrogen Storage in Destabilized Chemical Systems. *Scripta Mater.* **2007**, *56*, 829–834. [CrossRef]
35. Yu, X.B.; Guo, Y.H.; Sun, D.L.; Yang, Z.X.; Ranjbar, A.; Guo, Z.P.; Liu, H.K.; Dou, S.X. A Combined Hydrogen Storage System of $Mg(BH_4)_2-LiNH_2$with Favorable Dehydrogenation. *J. Phys. Chem. C* **2010**, *114*, 4733–4737. [CrossRef]
36. Bosenberg, U.; Kim, J.; Gosslar, D.; Eigen, N.; Jensen, T.; Colbe, J.B.V.; Zhou, Y.; Dahms, M.; Kim, D.; Günther, R. Role of Additives in $LiBH_4$–MgH_2 Reactive Hydride Composites for Sorption Kinetics. *Acta Mater.* **2010**, *58*, 3381–3389. [CrossRef]
37. Christian, M.L.; Aguey-Zinsou, K.F. Core–Shell Strategy Leading to High Reversible Hydrogen Storage Capacity for $NaBH_4$. *ACS Nano* **2012**, *6*, 7739–7751. [CrossRef]
38. Fujishima, A.; Honda, K. Electrochemical Photolysis of Water at a Semiconductor Electrode. *Nature* **1972**, *238*, 37–38. [CrossRef] [PubMed]
39. Lou, Z.; Zhu, M.; Yang, X.; Zhang, Y.; Whangbo, M.-H.; Li, B.; Huang, B. Continual Injection of Photoinduced Electrons Stabilizing Surface Plasmon Resonance of Non-Elemental-Metal Plasmonic Photocatalyst CdS/WO_{3-x} for Efficient Hydrogen Generation. *Appl. Catal. B Environ.* **2018**, *226*, 10–15. [CrossRef]
40. Ye, C.; Wang, R.; Wang, H.; Jiang, F. The High Photocatalytic Efficiency and Stability of $LaNiO_3$/g-C_3N_4 Heterojunction Nanocomposites for Photocatalytic Water Splitting to Hydrogen. *BMC Chem.* **2020**, *14*, 65. [CrossRef] [PubMed]
41. Tada, H.; Fujishima, M.; Kobayashi, H. Photodeposition of Metal Sulfide Quantum Dots on Titanium (IV) Dioxide and the Applications to Solar Energy Conversion. *Chem. Soc. Rev.* **2011**, *40*, 4232–4243. [CrossRef]
42. Jiang, D.; Wang, T.; Xu, Q.; Li, D.; Meng, S.; Chen, M. Perovskite Oxide Ultrathin with Significantly Enhanced Photocatalytic Activity towards the Photodegradation of Tetracycline. *Appl. Catal. B Environ.* **2017**, *201*, 617–628. [CrossRef]
43. Paramanik, L.; Reddy, K.H.; Sultana, S.; Parida, K. Architecture of biperovskite-based $LaCrO_3/PbTiO_3$ p–n heterojunction with a strong interface for enhanced charge anti-recombination process and visible light-induced photocatalytic reactions. *Inorg. Chem.* **2018**, *57*, 15133–15148. [CrossRef] [PubMed]
44. Li, J.; Zeng, J.; Jia, L.; Fang, W. Investigations on the Effect of Cu^{2+}/Cu^{+} Redox Couples and Oxygen Vacancies on Photocatalytic Activity of Treated $LaNi_{1-x}Cu_xO_3$ (x = 0.1, 0.4, 0.5). *Int. J. Hydrogen Energy* **2010**, *35*, 12733–12740. [CrossRef]
45. Wang, L.; Pang, Q.; Song, Q.; Pan, X.; Jia, L. Novel Microbial Synthesis of Cu Doped $LaCoO_3$ Photocatalyst and its Highly Efficient Hydrogen Production from Formaldehyde Solution under Visible Light Irradiation. *Fuel* **2015**, *140*, 267–274. [CrossRef]
46. Wang, J.; Cui, C.; Kong, Q.; Ren, C.; Li, Z.; Qu, L.; Zhang, Y.; Jiang, K. Mn-Doped g-C_3N_4 Nanoribbon for Efficient Visible-light Photocatalytic Water Splitting Coupling with Methylene Blue Degradation. *ACS Sustain. Chem. Eng.* **2018**, *6*, 8754–8761. [CrossRef]
47. Gupta, A.; Chemelewski, W.D.; Buddie Mullins, C.; Goodenough, J.B. High-rate Oxygen Evolution Reaction on Al-Doped $LiNiO_2$. *Adv. Mater.* **2015**, *27*, 6063–6067. [CrossRef]
48. Li, Y.; Hu, Y.; Fang, T.; Li, Z.; Zou, Z. Promoted Photoelectrochemical Activity of $BiVO_4$ coupled with $LaFeO_3$ and $LaCoO_3$. *Res. Chem. Intermediat.* **2018**, *44*, 1013–1024. [CrossRef]
49. Dhinesh Kumar, R.; Thangappan, R.; Jayavel, R. Synthesis and Characterization of $LaFeO_3/TiO_2$ Nanocomposites for Visible Light Photocatalytic Activity. *J. Phys. Chem. Solids* **2017**, *101*, 25–33. [CrossRef]

50. Ling, F.; Anthony, O.C.; Xiong, Q.; Luo, M.; Pan, X.; Jia, L.; Huang, J.; Sun, D.; Li, Q. PdO/$LaCoO_3$ Heterojunction Photocatalysts for Highly Hydrogen Production from Formaldehyde Aqueous Solution under Visible Light. *Int. J. Hydrogen Energy* **2016**, *41*, 6115–6122. [CrossRef]
51. Chu, J.; Han, X.; Yu, Z.; Du, Y.; Song, B.; Xu, P. Highly Efficient Visible-Light-Driven Photocatalytic Hydrogen Production on CdS/Cu_7S_4/g-C_3N_4 Ternary Heterostructures. *ACS Appl. Mater. Inter.* **2018**, *10*, 20404–20411. [CrossRef]
52. Yu, Q.; Meng, X.; Wang, T.; Li, P.; Liu, L.; Chang, K.; Liu, G.; Ye, J. A Highly Durable p-$LaFeO_3$/n-Fe_2O_3 Photocell for Effective Water Splitting under Visible Light. *Chem. Commun.* **2015**, *51*, 3630–3633. [CrossRef]
53. Jia, L.; Li, J.; Fang, W. Enhanced Visible-Light Active C and Fe Co-Doped $LaCoO_3$ for Reduction of Carbon Dioxide. *Catal. Commun.* **2009**, *11*, 87–90. [CrossRef]
54. Zhang, J.; Zhang, C.; Li, W.; Guo, Q.; Gao, H.; You, Y.; Li, Y.; Cui, Z.; Jiang, K.-C.; Long, H.; et al. Nitrogen-Doped Perovskite as a Bifunctional Cathode Catalyst for Rechargeable Lithium-Oxygen Batteries. *ACS Appl. Mater. Interfaces* **2018**, *10*, 5543–5550. [CrossRef] [PubMed]
55. Zhang, G.; Jiang, W.; Hua, S.; Zhao, H.; Zhang, L.; Sun, Z. Constructing Bulk Defective Perovskite $SrTiO_3$ Nanocubes for High Performance Photocatalysts. *Nanoscale* **2016**, *8*, 16963–16968. [CrossRef]
56. Yadav, A.A.; Hunge, Y.M.; Kang, S.-W. Porous Nanoplate-like Tungsten Trioxide/Reduced Graphene Oxide Catalyst for Sonocatalytic Degradation and Photocatalytic Hydrogen Production. *Surf. Interfaces* **2021**, *24*, 101075. [CrossRef]
57. Aksoy, M.; Metin, Ö. Pt Nanoparticles Supported on Mesoporous Graphitic Carbon Nitride as Catalysts for Hydrolytic Dehydrogenation of Ammonia Borane. *ACS Appl. Nano Mater.* **2020**, *3*, 6836–6846. [CrossRef]
58. Guo, X.; Chen, X.; Huang, Y.; Min, X.; Kong, C.; Tang, Y.; Liu, B. Atomically ordered Rh_2P catalysts anchored within hollow mesoporous carbon for efficient hydrogen production. *Chem. Commun.* **2021**, *57*, 12345–12348. [CrossRef] [PubMed]
59. Cheng, W.; Zhao, X.; Luo, W.; Zhang, Y.; Wang, Y.; Fan, G. Bagasse-derived Carbon-supported Ru nanoparticles as Catalyst for Efficient Dehydrogenation of Ammonia Borane. *ChemNanoMat* **2020**, *6*, 1251–1259. [CrossRef]
60. Liu, J.; Li, P.; Jiang, R.; Zheng, X.; Liu, P. Ru Nanoparticles Immobilized on Chitosan as Effective Catalysts for Boosting NH_3BH_3 Hydrolysis. *ChemCatChem* **2021**, *13*, 4142–4150. [CrossRef]
61. Paul, A.; Musgrave, C.B. Catalyzed Dehydrogenation of Ammonia–Borane by Iridium Dihydrogen Pincer Complex Differs from Ethane Dehydrogenation. *Angew. Chem.* **2007**, *119*, 8301–8304. [CrossRef]
62. Wang, C.; Zhao, J.; Du, X.; Sun, S.; Yu, X.; Zhang, X.; Lu, Z.; Li, L.; Yang, X. Hydrogen production from ammonia borane hydrolysis catalyzed by non-noble metal-based materials: A review. *J. Mater. Sci.* **2021**, *56*, 2856–2878. [CrossRef]
63. Zhan, W.-W.; Zhu, Q.-L.; Xu, Q. Dehydrogenation of Ammonia Borane by Metal Nanoparticle Catalysts. *ACS Catal.* **2016**, *6*, 6892–6905. [CrossRef]
64. Zhang, S.; Li, M.; Li, L.; Dushimimana, F.; Zhao, J.; Wang, S.; Han, J.; Zhu, X.; Liu, X.; Ge, Q.; et al. Visible-Light-Driven Multichannel Regulation of Local Electron Density to Accelerate Activation of O–H and B–H Bonds for Ammonia Borane Hydrolysis. *ACS Catal.* **2020**, *10*, 14903–14915. [CrossRef]
65. Xi, P.; Chen, F.; Xie, G.; Ma, C.; Liu, H.; Shao, C.; Wang, J.; Xu, Z.; Xu, X.; Zeng, Z. Surfactant Free RGO/Pd Nanocomposites as Highly Active Heterogeneous Catalysts for the Hydrolytic Dehydrogenation of Ammonia Borane for Chemical Hydrogen Storage. *Nanoscale* **2012**, *4*, 5597–5601. [CrossRef]
66. Alyami, N.M.; LaGrow, A.P.; Anjum, D.H.; Guan, C.; Miao, X.; Sinatra, L.; Yuan, D.-J.; Mohammed, O.F.; Huang, K.-W.; Bakr, O.M. Synthesis and Characterization of Branched fcc/hcp Ruthenium Nanostructures and their Catalytic Activity in Ammonia Borane Hydrolysis. *Cryst. Growth Des.* **2018**, *18*, 1509–1516. [CrossRef]
67. Zhang, J.; Wang, Y.; Zhu, Y.; Mi, G.; Du, X.; Dong, Y. Shape Selective Fabrication of Cu Nanostructures: Contrastive Study of Catalytic Ability for Hydrolytically Releasing H_2 from Ammonia Borane. *Renew. Energy* **2018**, *118*, 146–151. [CrossRef]
68. Yao, K.; Zhao, C.; Wang, N.; Li, T.; Lu, W.; Wang, J. An Aqueous Synthesis of Porous PtPd Nanoparticles with Reversed Bimetallic Structures for Highly Efficient Hydrogen Generation from Ammonia Borane Hydrolysis. *Nanoscale* **2020**, *12*, 638–647. [CrossRef] [PubMed]
69. Wang, Q.; Fu, F.; Yang, S.; Martinez Moro, M.; Ramirez, M.d.l.A.; Moya, S.; Salmon, L.; Ruiz, J.; Astruc, D. Dramatic Synergy in CoPt Nanocatalysts Stabilized by "Click" Dendrimers for Evolution of Hydrogen from Hydrolysis of Ammonia Borane. *ACS Catal.* **2019**, *9*, 1110–1119. [CrossRef]
70. Qu, X.; Jiang, R.; Li, Q.; Zeng, F.; Zheng, X.; Xu, Z.; Chen, C.; Peng, J. The Hydrolysis of Ammonia Borane Catalyzed by NiCoP/OPC-300 Nanocatalysts: High Selectivity and Efficiency, and Mechanism. *Green Chem.* **2019**, *21*, 850–860. [CrossRef]
71. Wang, C.; Tuninetti, J.; Wang, Z.; Zhang, C.; Ciganda, R.; Salmon, L.; Moya, S.; Ruiz, J.; Astruc, D. Hydrolysis of Ammonia Borane over Ni/ZIF-8 Nanocatalyst: High Efficiency, Mechanism, and Controlled Hydrogen Release. *J. Am. Chem. Soc.* **2017**, *139*, 11610–11615. [CrossRef]
72. Xu, P.; Lu, W.; Zhang, J.; Zhang, L. Efficient Hydrolysis of Ammonia Borane for Hydrogen Evolution Catalyzed by Plasmonic Ag@Pd Core–Shell Nanocubes. *ACS Sustain. Chem. Eng.* **2020**, *8*, 12366–12377. [CrossRef]
73. Yan, J.-M.; Zhang, X.-B.; Han, S.; Shioyama, H.; Xu, Q. Iron-Nanoparticle-Catalyzed Hydrolytic Dehydrogenation of Ammonia Borane for Chemical Hydrogen Storage. *Angew. Chem. Int. Edit.* **2008**, *47*, 2287–2289. [CrossRef]
74. Metin, Ö.; Mazumder, V.; Özkar, S.; Sun, S. Monodisperse Nickel Nanoparticles and Their Catalysis in Hydrolytic Dehydrogenation of Ammonia Borane. *J. Am. Chem. Soc.* **2010**, *132*, 1468–1469. [CrossRef] [PubMed]

75. Hu, J.; Chen, Z.; Li, M.; Zhou, X.; Lu, H. Amine-Capped Co Nanoparticles for Highly Efficient Dehydrogenation of Ammonia Borane. *ACS Appl. Mater. Interfaces* **2014**, *6*, 13191–13200. [CrossRef]
76. Li, D.; Wehrung, J.-F.; Zhao, Y. Gold Nanoparticle-Catalyzed Photosensitized Water Reduction for Hydrogen Generation. *J. Mater. Chem. A* **2015**, *3*, 5176–5182. [CrossRef]
77. Kumaravel, V.; Imam, M.; Badreldin, A.; Chava, R.; Do, J.; Kang, M.; Abdel-Wahab, A. Photocatalytic Hydrogen Production: Role of Sacrificial Reagents on the Activity of Oxide, Carbon, and Sulfide Catalysts. *Catalysts* **2019**, *9*, 276. [CrossRef]
78. Yang, Y.W.; Lu, Z.H.; Hu, Y.J.; Zhang, Z.J.; Shi, W.M.; Chen, X.S.; Wang, T.T. Facile in situ Synthesis of Copper Nanoparticles Supported on Reduced Graphene Oxide for Hydrolytic Dehydrogenation of Ammonia Borane. *RSC Adv.* **2014**, *4*, 13749–13752. [CrossRef]
79. Li, J.L.; Ren, X.Y.; Lv, H.; Wang, Y.Y.; Li, Y.F.; Liu, B. Highly Efficient Hydrogen Production from Hydrolysis of Ammonia Borane Over Nanostructured Cu@CuCoO$_x$ Supported on Graphene Oxide. *J. Hazard. Mater.* **2020**, *391*, 122199. [CrossRef] [PubMed]
80. Yamada, Y.; Yano, K.; Xu, Q.; Fukuzumi, S. Cu/Co_3O_4 Nanoparticles as Catalysts for Hydrogen Evolution from Ammonia Borane by Hydrolysis. *J. Phys. Chem. C* **2010**, *114*, 16456–16462. [CrossRef]
81. Yao, Q.L.; Huang, M.; Lu, Z.H.; Yang, Y.W.; Zhang, Y.X.; Chen, X.S.; Yang, Z. Methanolysis of Ammonia Borane by Shape-Controlled Mesoporous Copper Nanostructures for Hydrogen Generation. *Dalton Trans.* **2015**, *44*, 1070–1076. [CrossRef] [PubMed]
82. Lu, Z.H.; Li, J.P.; Zhu, A.L.; Yao, Q.L.; Huang, W.; Zhou, R.Y.; Zhou, R.F.; Chen, X.S. Catalytic Hydrolysis of Ammonia Borane *via* Magnetically Recyclable Copper Iron Nanoparticles for Chemical Hydrogen Storage. *Int. J. Hydrogen Energy* **2013**, *38*, 5330–5337. [CrossRef]
83. Qin, X.; Liu, X.W.; Hua, W.; Bettinelli, M.; Liu, X.G. Lanthanide-Activated Phosphors Based on 4f–5d Optical Transitions: Theoretical and Experimental Aspects. *Chem. Rev.* **2017**, *117*, 4488–4527. [CrossRef]
84. Zhou, B.; Shi, B.Y.; Jin, D.Y.; Liu, X.G. Controlling Upconversion Nanocrystals for Emerging Applications. *Nat. Nanotechnol.* **2015**, *10*, 924–936. [CrossRef]
85. Qin, X.; Xu, J.H.; Wu, Y.M.; Liu, X.G. Energy-Transfer Editing in Lanthanide-Activated Upconversion Nanocrystals: A Toolbox for Emerging Applications. *ACS Cent. Sci.* **2019**, *5*, 29–42. [CrossRef] [PubMed]
86. Zhou, J.; Liu, Q.; Feng, W.; Sun, Y.; Li, F.Y. Upconversion Luminescent Materials: Advances and Applications. *Chem. Rev.* **2015**, *115*, 395–465. [CrossRef] [PubMed]
87. Chen, G.Y.; Qju, H.L.; Prasad, P.N.; Chen, X.Y. Upconversion Nanoparticles: Design, Nanochemistry, and Applications in Theranostics. *Chem. Rev.* **2014**, *114*, 5161–5214. [CrossRef] [PubMed]
88. Dong, H.; Du, S.R.; Zheng, X.Y.; Lyu, G.M.; Sun, L.D.; Li, L.D.; Zhang, P.Z.; Zhang, C.; Yan, C.H. Lanthanide Nanoparticles: From Design toward Bioimaging and Therapy. *Chem. Rev.* **2015**, *115*, 10725–10815. [CrossRef]
89. Snoke, D.; Wolfe, J.P.; Mysyrowicz, A. Quantum Saturation of a Bose-Gas; Excitons in Cu_2O. *Phys. Rev. Lett.* **1987**, *59*, 827–830. [CrossRef]
90. Snoke, D. Coherent Exciton Waves. *Science* **1996**, *273*, 1351–1352. [CrossRef]
91. Jolk, A.; Klingshirn, C.F. Linear and Nonlinear Excitonic Absorption and Photoluminescence Spectra in Cu_2O: Line Shape Analysis and Exciton Drift. *Phys. Status Solidi B* **1998**, *206*, 841–850. [CrossRef]
92. Zou, Y.T.; Hu, Y.Z.; Uhrich, A.; Shen, Z.W.; Peng, B.X.; Ji, Z.Y.; Muhler, M.; Zhao, G.X.; Wang, X.K.; Xu, X.X. Steering Accessible Oxygen Vacancies for Alcohol Oxidation Over Defective Nb_2O_5 Under Visible Light Illumination. *Appl. Catal. B.* **2021**, *298*, 120584. [CrossRef]
93. Li, B.F.; Hong, J.H.; Ai, Y.J.; Hu, Y.Z.; Shen, Z.W.; Li, S.J.; Zou, Y.T.; Zhang, S.; Wang, X.K.; Zhao, G.X.; et al. Visible-Near-Infrared-Light-Driven Selective Oxidation of Alcohols Over Nanostructured Cu Doped $SrTiO_3$ in Water Under Mild Condition. *J. Catal.* **2021**, *399*, 142–149. [CrossRef]
94. Zhang, K.Y.; Xi, Z.S.; Wu, Z.Y.; Lu, G.L.; Huang, X.B. Visible-Light-Induced Selective Oxidation of Amines into Imines Over UiO-66-NH_2@Au@COF Core-Shell Photocatalysts. *ACS Sustain. Chem. Eng.* **2021**, *9*, 12623–12633. [CrossRef]
95. Lu, G.L.; Huang, X.B.; Li, Y.; Zhao, G.X.; Pang, G.S.; Wang, G. Covalently Integrated Core-Shell MOF@COF Hybrids as Efficient Visible-Light-Driven Photocatalysts for Selective Oxidation of Alcohols. *J. Energy Chem.* **2020**, *43*, 8–15. [CrossRef]